LEVEL II



VSC-TR-81-28

# THREE-DIMENSIONAL FINITE DIFFERENCE SIMULATION OF FAULT DYNAMICS: RECTANGULAR FAULTS WITH FIXED RUPTURE VELOCITY

S. M. Day

TOPICAL REPORT

SYSTEMS, SCIENCE AND SOFTWARE
P.O. Box 1620
La Jolla, California 92038

September 1981



Monitored by:

VELA Seismological Center
312 Montgomery Street
Alexandria, VA 22314

Unclassified

SECURITY CLASSIFICATION OF THIS PAGE (When Data Entered)

| REPORT DOCUMENTATION PAGE | READ INSTRUCTIONS BEFORE COMPLETING FORM |
|---|---|
| 1. REPORT NUMBER: VSC-TR-81-28 | 2. GOVT ACCESSION NO.: AD-A110064 |
| 3. RECIPIENT'S CATALOG NUMBER: | |
| 4. TITLE (and Subtitle): Three-Dimensional Finite Difference Simulation of Fault Dynamics: Rectangular Faults with Fixed Rupture Velocity | 5. TYPE OF REPORT & PERIOD COVERED: Topical Report |
| | 6. PERFORMING ORG. REPORT NUMBER: SSS-R-81-5158 |
| 7. AUTHOR(s): S. M. Day | 8. CONTRACT OR GRANT NUMBER(s): F08606-79-C-0008 |
| 9. PERFORMING ORGANIZATION NAME AND ADDRESS: Systems, Science and Software, P. O. Box 1620, La Jolla, California 92038 | 10. PROGRAM ELEMENT, PROJECT, TASK AREA & WORK UNIT NUMBERS: Program Code No. 6H189, ARPA Order No. 2551 |
| 11. CONTROLLING OFFICE NAME AND ADDRESS: VELA Seismological Center, 312 Montgomery Street, Alexandria, Virginia 22314 | 12. REPORT DATE: September 1981 |
| | 13. NUMBER OF PAGES: 45 |
| 14. MONITORING AGENCY NAME & ADDRESS (if different from Controlling Office) | 15. SECURITY CLASS. (of this report): Unclassified |
| | 15a. DECLASSIFICATION/ DOWNGRADING SCHEDULE |

16. DISTRIBUTION STATEMENT (of this Report)

Approved for Public Release, Distribution Unlimited.

17. DISTRIBUTION STATEMENT (of the abstract entered in Block 20, if different from Report)

18. SUPPLEMENTARY NOTES

19. KEY WORDS (Continue on reverse side if necessary and identify by block number)

Earthquakes, finite difference, dynamic modeling, three-dimensional

20. ABSTRACT (Continue on reverse side if necessary and identify by block number)

We analyze three-dimensional finite difference solutions for a simple shear-crack model of faulting to determine the effects of fault length and width on the earthquake slip function. The fault model is dynamic, with only rupture velocity, fault dimensions, and dynamic stress-drop prescribed. The numerical solutions are accurate for frequencies up to 5 Hz, and are combined with asymptotic results for shear cracks in order to characterize the slip function at higher frequencies.

(continued)

DD FORM 1 JAN 73 1473 EDITION OF 1 NOV 65 IS OBSOLETE

Unclassified

SECURITY CLASSIFICATION OF THIS PAGE (When Data Entered)

(continued)

Near the hypocenter, the slip velocity exhibits a square root singularity whose intensity increases with hypocentral distance. At distances greater than the fault width, w, growth of the velocity intensity ceases, and the slip function becomes nearly invariant with distance along the fault length. Close-form expressions are developed for the dependence of static slip ($s_\infty$), slip rise time ($T_R$), and slip velocity intensity ($V$) on fault geometry. Along the centerline of a long, narrow fault, at hypocentral distances exceeding w, these expressions reduce to $s_\infty \approx w\Delta\tau/\mu$, $T_R \approx 0.5\ w/\upsilon_R$, and $V \approx \sqrt{w/2}\ \upsilon_R\ \Delta\tau/\mu$, where $\Delta\tau$ is the dynamic stress drop, $\mu$ the shear modulus, and $\upsilon_R$ the rupture velocity.

The numerical results imply that uniform-dislocation kinematic earthquake models in which slip is represented by a ramp time-function will underpredict high-frequency ground motion relative to low-frequency ground motion. A further implication of the numerical solutions is that the nature of inelastic processes at the advancing edge of a long fault will depend on fault width, but will be independent of rupture length.

AFTAC Project Authorization No. VT/0712/B/PMP
ARPA Order No. 2551, Program Code No. 6H189
Effective Date of Contract: November 17, 1978
Contract Expiration Date: November 15, 1981
Amount of Contract: $1,816,437
Contract No. F08606-79-C-0008
Principal Investigator and Phone No.
Dr. J. Theodore Cherry, (714) 453-0060
Project Scientist and Phone No.
Mr. Brian W. Barker, (202) 325-7581

This research was supported by the Advanced Research Projects Agency of the Department of Defense and was monitored by AFTAC/VSC, Patrick Air Force Base, Florida 32925, under Contract No. F08606-79-C-0008.



W/O 11098

TABLE OF CONTENTS

## LIST OF ILLUSTRATIONS

# I. INTRODUCTION

Deterministic simulation of earthquake ground motion has played an increasingly important role in seismology and earthquake engineering in recent years. For example, ground motion simulation has been used recently as a tool for developing engineering design motion criteria (Wiggins, et al., 1978; Apsel, 1979). Such simulations require theoretical models for both the source process and the propagation and dissipation of seismic energy. While ground motion simulations have been undertaken using rather rigorous theoretical methods to model anelastic wave propagation from source to site, including the effects of depth-dependent geologic structure, the earthquake source itself is usually specified on largely intuitive grounds. The displacement-discontinuity time history (slip function), by means of which the earthquake source is represented, is generally prescribed without rigorous consideration of fault dynamics.

Following Haskell (1964; 1969) and Savage (1966), most studies have represented the earthquake by a slip function which is spatially uniform over the fault surface and has some simple time dependence, usually that of a finite-duration ramp. Simple kinematic source models of this type have proven useful for representing low-frequency (less than about 1 Hz) characteristics of earthquake ground motion. For example, Bouchon (1979) used a uniform dislocation of ramp form in combination with a layered earth structure to model the Station 2 velocity and displacement recordings of the 1966 Parkfield earthquake. However, high frequency (1 to 20 Hz) ground motion is highly sensitive to the specification of the source process. The analysis of Madriaga (1978), in particular, underscores the inapproriateness of the uniform-slip kinematic models for synthesizing ground motion with wavelengths much shorter than the fault width. This high frequency radiation is important in earthquake engineering, as well as in nuclear monitoring studies.

Closed-form theoretical solutions describing the slip function are available only for the most idealized dynamic shear-crack models of earthquakes. Restricting consideration to three-dimensional analyses, perhaps the most useful of such analytical results are the solutions of Kostrov (1964) and Burridge and Willis (1969). The former gives the slip history on a circular shear crack which initiates at a point in a prestressed whole space and grows at a fixed rupture velocity without stopping; the latter extends Kostrov's result to the case of an elliptical shear crack. These self-similar solutions are characterized by square-root singularities at the crack edge in both shear stress and slip velocity, and the intensity of these singularities grows as the crack dimension increases. While these analytic solutions are very useful for interpreting the results of more complex numerical studies, they cannot account for effects associated with the stopping of rupture growth and the ensuing arrest of slip.

Madariaga (1977a) used two-dimensional analytical results, notably those of Kostrov (1966, 1975) and Fossum and Freund (1975) to characterize the slip-velocity singularities associated with the starting and stopping of ruptures. He then applied a representation theorem, together with Keller's (1962) geometric theory of diffraction to construct a high-frequency approximation for the radiation from shear cracks in three dimensions. This analysis yields expressions for the radiation from a discrete jump in rupture velocity. The solution involves a stress intensity factor which depends on the three-dimensional geometry of the fault as well as its stress and rupture history, and a second factor which depends only on the instantaneous jump in rupture velocity along the crack edge. The solution in this form provides considerable insight into the process of high-frequency generation, although to fully characterize the stress intensity factor and rupture velocity, a complete solution to the three-dimensional dynamical problem would still be required.

In general, numerical methods are necessary to solve the three-dimensional dynamic problem of a fault which stops. Several studies have addressed this problem, with the approximation that rupture velocity is specified a priori. This fixed-rupture-velocity fault model has been studied for faulting confined to a circular region (Madariaga, 1976; Das, 1980), a semi-circular region (Archuleta and Frazier, 1978), and rectangular regions (Madariaga, 1977b, 1979; Day, 1979; Archuleta and Day, 1980). Das (1981) and Day (1979) have studied rectangular faults in which rupture velocity is derived from a fracture criterion (spontaneous rupture). These numerical solutions demonstrate that edge effects associated with the narrow dimension of the fault substantially influence the slip function, controlling static slip and slip rise time.

In this study, our objective is to provide an improved understanding of three-dimensional geometrical effects governing slip functions. The study employs three-dimensional finite-difference solutions to the dynamic fault problem in a whole space. On the basis of the numerical solutions, closed-form approximations are derived for the static slip and rise time predicted for rectangular faults. These quantities are measures of the low- to intermediate-frequency content of the slip function. A particular emphasis of this study, however, will be to quantify the high-frequency behavior of the slip function, which has been largely unresolvable from previous numerical studies of earthquake dynamics. It is the high-frequency character (greater than 1 Hz or so) of the slip function which is of primary importance for synthesizing near-field ground motion in the period range of engineering interest. The high-frequencies are also of importance for synthesizing earthquake ground motion at regional distances, where substantial seismic energy is recorded in the 1-5 Hz range. A good source model for high frequencies is also important for inferring the attentuative properties of teleseismic propagation paths (i.e., t*). Furthermore, some of the methods proposed for discriminating earthquakes from underground explosions use spectral characteristics

of telesismic P-waves in the 1-5 Hz range (e.g., Bache, et al., 1979). Once the high-frequency behavior of the slip function has been quantified from the numerical solutions, the numerical results are combined with asymptotic results for dynamic cracks, in order to characterize the stress intensity and energy release rate at the advancing fault edges.

So as to focus our analysis on the geometrical effects associated with the three-dimensionality of the problem, we employ the approximation that rupture velocity be a specified constant. The finite difference method used here is, of course, also well suited to the more complex problem of modeling spontaneous rupture propagation.

The finite difference computations on which this analysis is based were performed on the ILLIAC IV computer at NASA/Ames Research Center. Programming support was provided under the direction of Susan Biester and Stewart Hopkins.

# II. THE FAULT MODEL

## 2.1 INTRODUCTION

In the earthquake simulations reported here, we treat faulting as a propagating shear stress relaxation which occurs as a consequence of shear failure on a planar surface. The mathematical formulation follows closely that of Equations 2.1 to 2.13 of Kostrov (1970). Archuleta and Frazier (1978) also present a detailed exposition of a mathematical model of a propagating shear stress relaxation.

We will specify the initial state of stress in the medium, its constitutive properties, the rupture velocity, the limiting edge of the rupture surface, and the friction law to be satisfied on the rupture surface after failure. Although the velocity of the rupture front is prescribed, the time of arrest of slip at a given point is not. Instead, the cessation of slip is a consequence of the nonlinear friction law, and is determined as a part of the dynamic solution.

## 2.2 INITIAL CONDITIONS AND CONSTITUTIVE PROPERTIES

For time t less than zero, we assume that an equilibrium state of stress exists with velocity everywhere zero. The equilibrium configuration is such that the prospective fault plane experiences a uniform shear traction $\tau_o$ and compressional normal traction $\sigma_N$.

The fault plane is permitted to fail in shear, but the medium will otherwise be assumed to be linearly elastic. Since average stress changes associated with faulting are modest, on the order of a few hundred bars, linear elasticity is a reasonable model of material behavior away from the immediate zone of faulting.

## 2.3 GROWTH OF THE RUPTURE

The rupture surface is assumed to occupy a prescribed plane with unit normal vector $\underline{\hat{n}}$. We specify the growth of the fault surface as a function of time, rather than determining its evolution

from the dynamic solution via some failure model. The rupture nucleates at a point and expands symmetrically at a constant, prescribed rupture velocity $v_R$, until it reaches a prescribed rectangular boundary (Figure 1). $\Sigma(t)$ denotes the portion of the plane which has ruptured by time t; w and $\ell$ denote the width and length of a rectangular fault, and x and y are Cartesian coordinates on the fault plane. Then $\Sigma(t)$ consists of all points x, y such that:

$$x^2 + y^2 < v_R^2 t^2 \quad ,$$

$$|x| \leq \frac{\ell}{2} \quad ,$$

and $$|y| \leq \frac{w}{2} \quad .$$

Two somewhat artificial features of this rupture model require mention. They are: 1) the instantaneous acceleration of the rupture to its terminal velocity, and (2) the instantaneous deceleration of rupture velocity to zero along a prescribed boundary. The former assumption may be a fairly good approximation. There is both experimental (Wu, et al., 1972: Archuleta and Brune, 1975) and theoretical (Cherry, et al., 1976; Das and Aki, 1977) evidence that rupture velocity can accelerate very rapidly to its terminal value.

The approximation of abrupt stopping, on the other hand, is difficult to support experimentally, since ruptures normally propagate completely through laboratory samples. While the approximation of abrupt stopping may be quite artificial, it is not precluded by theories of dynamic crack propagation. For example, Husseini et al., (1975) have shown that a rupture can stop instantaneously when it encounters jumps in fracture energy on the fault plane. This reflects the fact that a crack edge, at least in the linearly-elastic continuum theory, lacks "inertia". That is, the stresses immediately ahead of the crack edge depend on rupture velocity, but not on the time derivatives of rupture velocity (Eshelby, 1969).

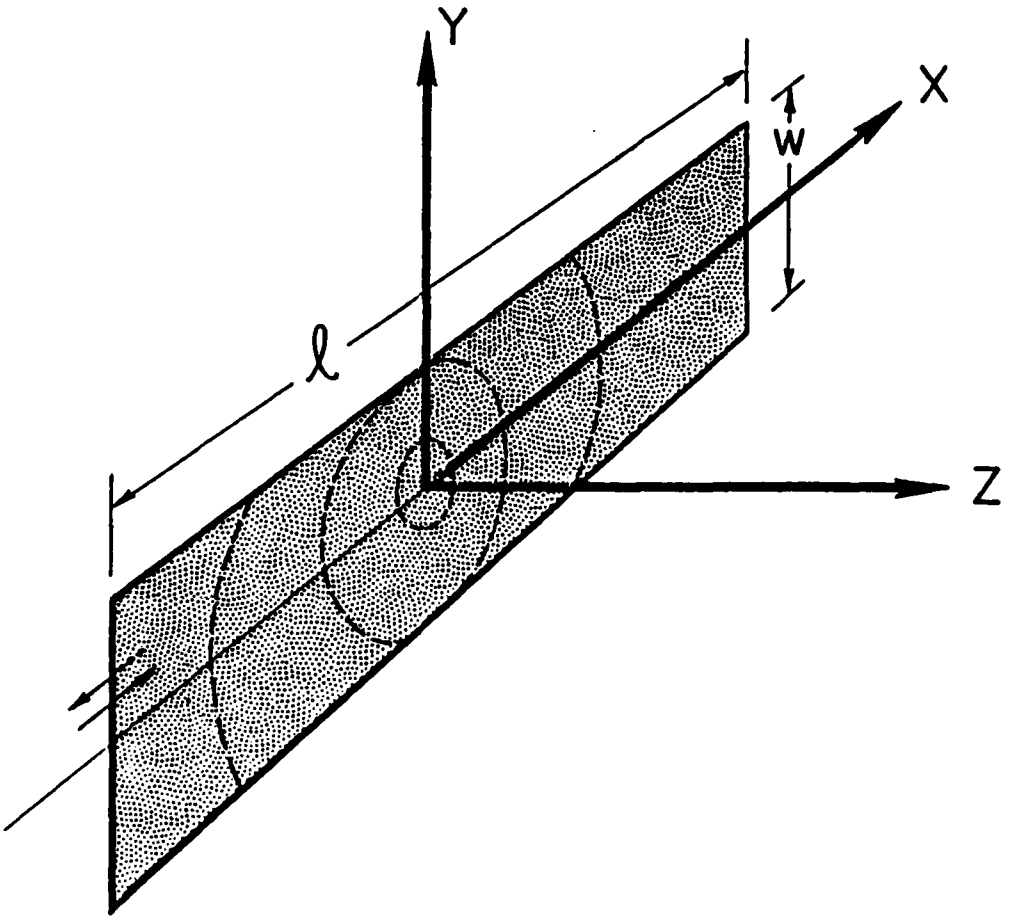


Figure 1. Rupture geometry and coordinate system for the numerical simulations. The shear prestress is in the x direction on the plane z = 0. Rupture initiates at the origin and expands symmetrically at fixed rupture velocity.

The importance of the mode of stopping lies in its consequences for high-frequency radiation. Madariaga (1977a) has shown that the strongest radiation of high-frequencies is associated with abrupt changes in rupture velocity such as the sudden stopping at the fault edges in our Model. A rupture velocity jump generates $f^{-2}$ high-frequency behavior of the far-field displacement spectrum, in contrast to the starting phase, which (assuming nucleation at a point) generates at most an $f^{-3}$ spectral asymptote.

## 2.4 BOUNDARY CONDITION OF THE FAULT

On $\Sigma(t)$, we permit a tangential displacement discontinuity (slip) $\underline{s}(\underline{x},t)$, and require continuity of the traction vector and of the normal component of displacement. The shear traction on $\Sigma$ obeys a simple Coulomb friction law. The physical requirements of this friction law are: i) the magnitude of the shear traction on $\Sigma$ is bounded by a prescribed sliding friction value which depends only on the normal traction, and, ii) the shear traction is equal in magnitude to the sliding friction value and opposite in direction to the slip velocity vector whenever the latter is non-zero.

The vector $\underline{\tau}$ denotes the shear traction exerted on the positive side of $\Sigma$ by the negative side (where the direction of $\hat{n}$ is from the negative side of $\Sigma$ toward the positive). We define $\underline{\tau}_f$ to be a sliding frictional traction whose direction opposes the instantaneous slip velocity and whose amplitude is proportional to the normal traction on $\Sigma$:

$$\underline{\tau}_f = -\tau_f \frac{\dot{\underline{s}}}{|\dot{\underline{s}}|} ,$$

where $\tau_f$ is $-\mu_d \sigma_N$, the product of the normal traction and the coefficient of dynamic friction. The amplitude of the sliding friction, $\tau_f$, is presumed to be positive, constant, and less than the absolute value of the shear prestress $\tau_0$, so that a stress drop occurs at the rupture front. We then define $\underline{\tau}_c$ to be the

shear traction, at a point on $\Sigma$, which would be sufficient to enforce continuity of velocity. That is, $\underline{\tau}_c$ is the instantaneous shear traction which would accompany healing, a quantity which can be readily determined at any time step from the numerical solution. Then the following boundary condition on $\Sigma$ is equivalent to the friction law described in the last paragraph:

$$\underline{\tau} = \begin{cases} \underline{\tau}_f & \text{if } |\underline{\tau}_c| > \tau_f \\ \underline{\tau}_c & \text{if } |\underline{\tau}_c| \leq \tau_f \end{cases} . \qquad (1)$$

Equation (1) ensures that the slip velocity $\underline{\dot{s}}$ is non-zero only if the magnitude of $\underline{\tau}$ would otherwise exceed that of sliding friction, $\tau_f$.

Note from Equation (1) that we do not assume that the frictional stress immediately increases above the dynamic friction value $\tau_f$ when a slip velocity zero occurs. Rather than assuming instantaneous recovery of strength, we let $\tau_f$ continue to bound the shear stress on the fault, even after the slip velocity goes to zero. This is in accord with results from laboratory studies of time-dependent rock friction. For example, Dieterich (1972, 1978) found frictional strength of rock surfaces to be proportional to the logarithm of their time of contact, with essentially no recovery of strength occuring during the first one second of contact. Thus, any increase of frictional strength due to stationary contact should be negligible on the time scale of dynamic rupture.

## 2.5 STRESS-DROP SCALING

The dynamic stress-drop, $\Delta\tau$, is defined here as the difference between the absolute values of shear prestress and sliding frictional stress,

$$\Delta\tau = \tau_0 - \tau_f .$$

This quantity is the stress available to accelerate the fault slip, and has also been termed "effective stress" in the seismological

literature (e.g., Brune, 1970). If the slip direction were constrained to be parallel to the direction of the prestress, then the dynamic solution would scale directly with the assumed value of $\Delta\tau$, and would be independent of $\tau_f$. This constraint of the slip direction is equivalent to assuming $\tau_f >> \Delta\tau$. In the current study, we have made this simplifying assumption so that the numerical results can be scaled rigorously with $\Delta\tau$. The assumption $\tau_f >> \Delta\tau$ is consistent with laboratory studies of stick-slip, which report fractional stress drops, $\Delta\tau/\tau_0$, of a few percent to a few tens of percent (for example, Byerlee, 1967; Scholz, et al., 1972; Dieterich, et al., 1978).

Actually, this simplification does not have a significant effect on the solution (apart from inhibiting slip reversal as discussed below). It is known, for example, that the self-similar, expanding elliptical crack exhibits slip which is everywhere parallel to the prestress direction, even for the case of zero friction (Burridge and Willis, 1969). For finite faults with low friction, stopping of rupture can introduce a component of slip perpendicular to the prestress direction. However, Madariaga (1976) has shown, for the case of a finite circular crack, that this component is quite small. So, scaling with $\Delta\tau$, while rigorous only for $\tau_f >> \Delta\tau$, should be a good approximation even for relatively low values of $\tau_f$.

## 2.6 HEALING

When the slip velocity at a point goes to zero, Equation (1) provides the criterion for whether to permit further slip. Recommencement of slip is prohibited by Equation (1) if such slip (which must be accompanied by a shear traction of magnitude $\tau_f$) would increase the magnitude of the shear traction $\underline{\tau}$, rather than decrease it since that would violate our physical assumption that the shear traction on $\Sigma$ opposes the slip velocity.

Although the friction law embodied in Equation (1) does not automatically preclude a reversal of sliding direction, a reversal could only occur for very small values of sliding friction in this model. We define the overshoot stress as the amount by which the shear traction, at a point on $\Sigma$, drops below $\tau_f$ after sliding ceases. In order for sliding to reverse, the shear traction would have to drop from the sliding friction value to zero, then reverse sign and increase in magnitude back to $\tau_f$; so no sliding reversal will occur unless $\tau_f$ is less than half the overshoot stress. The numerical results given in the next section show that the overshoot does not exceed about 26 percent of the dynamic stress drop; therefore, a sliding reversal would only occur if the fractional stress drop $\Delta\tau/\tau_0$ were at least 0.88. Since we have assumed $\tau_f >> \Delta\tau$ (i.e., very small fractional stress drop), sliding reversal does not occur in our simulations.

# III. NUMERICAL SOLUTIONS FOR THE FAULT SLIP

## 3.1 METHOD OF SOLUTION

The mathematical model of faulting outlined in the last section poses a three-dimensional, nonlinear, mixed boundary value problem. To determine the fault slip, this problem is solved numerically using a three-dimensional finite difference method developed by Cherry (1977), in which explicit time stepping is used to integrate the dynamic solution in time. Equation 1, governing the fault plane, was discretized in accordance with the method developed by Day (1977, Appendix IV).

## 3.2 DESCRIPTION OF THE CALCULATIONS

We present slip functions obtained from numerical simulations of four different fault geometries. Each calculation simulates a rectangular fault surface in a uniform whole space. In each case, rupture initiates at the center of the rectangle, as in Figure 1, and the prestress direction is aligned with the long dimension of the fault.

The numerical results have been scaled to represent the following set of physical parameters:

P wave speed, $\alpha$ = 6.0 km/sec
S wave speed, $\beta$ = 3.46 km/sec
shear modulus, $\mu$ = 3.24 x $10^{11}$ dynes/cm
rupture velocity, $v_R$ = 3.12 km/sec
dynamic stress drop, $\Delta\tau$ = 100 bars

Three of the calculations represent a fault length $\ell$ of 8 km and fault widths w of 1.5, 4, and 8 km, respectively. The fourth calculation was for a fault length of 16 km and a fault width of 4 km. The solutions may be rescaled to represent a different set of material and fault parameters, provided Poisson's ratio, the fault aspect ratio, and the ratio $v_R/\beta$ are unchanged. The appropriate

scaling relationships have been summarized by Madariaga (1976), and we repeat them here for convenience. Assume that the above values of dynamic stress drop, fault width, shear speed, and shear modulus are multiplied by factors $\Delta\tau'$, $w'$, $\beta'$, and $\mu'$, respectively. Then, time, length, stress and displacment in the numerical solutions are to be multiplied by scale factors $t'$, $x'$, $\sigma'$ and $u'$, respectively:

$$\text{(time)} \qquad t' = \frac{w'}{\beta'}$$

$$\text{(Length)} \qquad x' = w'$$

$$\text{(Stress)} \qquad \sigma' = \Delta\tau'$$

$$\text{(Displacement)} \qquad u' = \frac{\Delta\tau'}{\mu'} w' \quad .$$

In rescaling the numerical solutions, however, consideration must be given to a hidden length scale in the problem, the finite difference cell dimension. The main limitation of the finite difference method is that the discretization causes substantial numerical dispersion of wavelengths shorter than about 6 cell dimensions. Consequently, accuracy is degraded for high-frequency components of the solution. For these four finite difference calculations, the mesh refinement was sufficient to retain accuracy for frequency components up to about 5 Hz. Frequencies higher than 5 Hz have therefore been removed from the solutions using a combination of artificial viscosity and post-processing with a low-pass digital filter. This non-physical cutoff frequency scales as $\beta/w$.

## 3.3 SLIP TIME-HISTORIES

Figure 2 shows the calculated slip histories for selected points along the fault length for the square (8 km by 8 km) fault. The final offset is greatest near the center of the fault, decreasing as the observation point approaches an edge. The rise time of the slip function is also greatest at the center, where it equals approximately the fault length divided by the shear speed. The rise time decreases as the edges of the fault are approached.

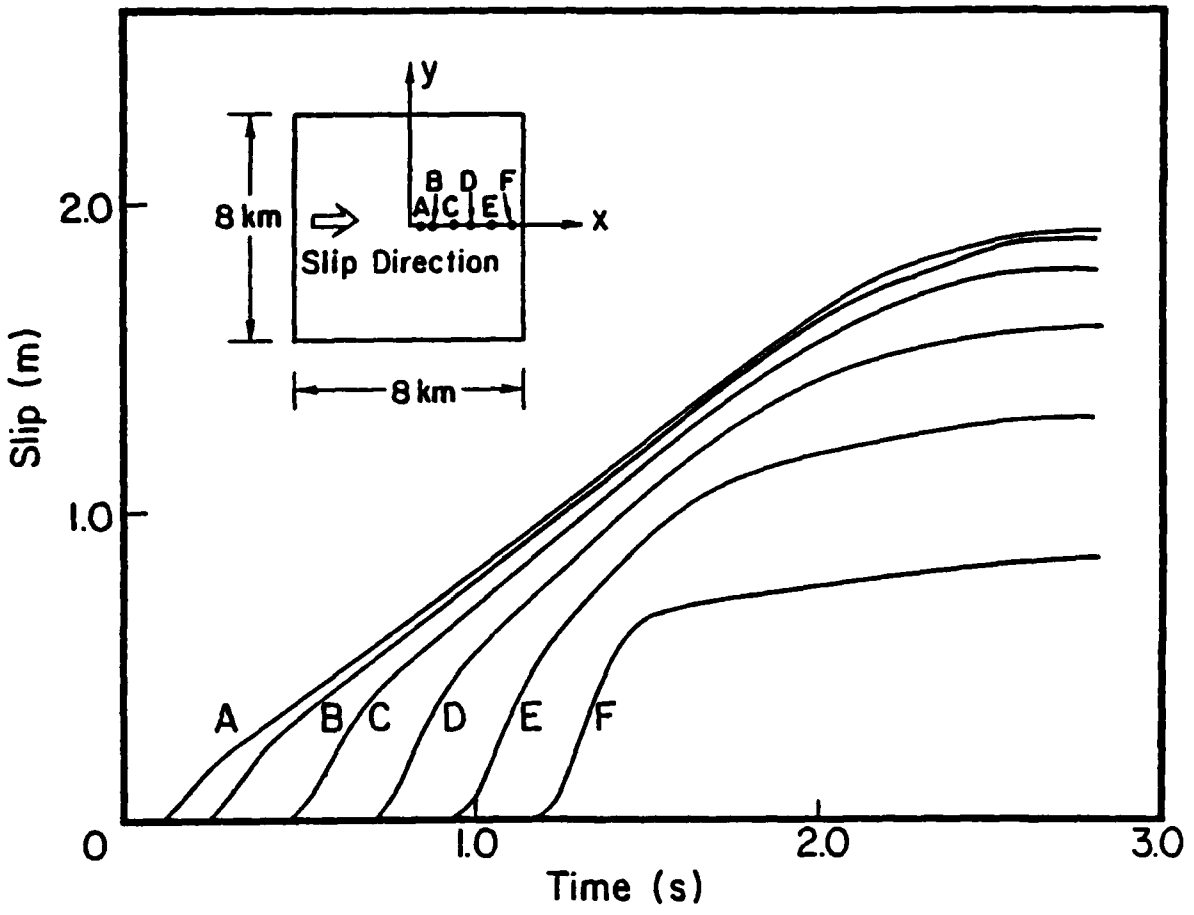


Figure 2. Computed slip time-histories along the center-line of the square fault plane at several distances from the hypocenter. Slip is scaled to represent a dynamic stress drop of 100 bars and a fault length of 8 km.

Arrest of slip occurs first at the outer edge and propogates inward. The center of the fault is the last point to heal. Overall, the healing behavior is very similar to that of the circular fault, as obtained by Madariaga (1976), in spite of the reduced symmetry present in the square fault problem (the circular fault stops simultaneously everywhere on its perimeter whereas the square fault does not).

We can compare the residual slip for the square fault to Neuber's (1937) static solution for a circular shear crack in a Poisson solid, for which the slip s is

$$s(r) = \frac{24}{7\pi} \frac{\Delta\tau}{\mu} a \, (1-r^2/a^2)^{1/2} \quad , \qquad (2)$$

where a is the crack radius and r is the distance to the center of the crack. For the circular crack, the average static slip, from Equation 2, is 2/3 times the static slip at the center. For the square fault calculation, the average static slip is found to be 0.65 times the static slip at the center, which is nearly identical to the circular fault relationship.

As a reasonable approximation, we might apply Equation 2 to the square fault with the reinterpretation that a is $\sqrt{A/\pi}$ , where A is the fault area. In that case, the static offset at the center of the square fault exceeds the prediction of Equation 2 by a factor of 1.26. This "overshoot" of the dynamic solution relative to the static solution has been discussed for circular faults by Madariaga (1976), Archuleta (1976), and Das (1980). The value of 1.26 obtained here for the square fault is in good agreement with their numerical results (which range from 1.20 to 1.27).

This value of overshoot implies that no reversal in slip direction will occur if the dynamic frictional traction $\tau_f$ exceeds about 0.13 $\Delta\tau$, or half the overshoot stress. Thus, as remarked in the previous section, a slip reversal requires a fractional stress drop, $\Delta\tau/\tau_0$, greater than 0.88, which is far greater than those observed in laboratory stick-slip experiments. We emphasize again

that this conclusion requires only our assumption that sliding friction is a dissipative process which opposes the slip; it does not require an assumption of rapid strength recovery on the fault following a slip velocity zero.

Figure 3 shows slip histories calculated along the fault length for the case $w = 4$ , $\ell = 8$. The time histories in this case are similar to those in Figure 2, but the rise time and static slip are reduced, especially near the center of the fault. Rise time and static slip at a point are apparently controlled by proximity of the nearest edge of the fault.

Figure 4 shows slip histories for the case $w = 1.5$, $\ell = 8$. Again, it is clear that fault width controls static amplitude and rise time. Beyond a distance of about one fault width from the hypocenter, the slip function remains essentially constant in shape with increasing hypocentral distance. This uniformity of the slip function beyond one fault width is also apparent in Figure 5 for the case $w = 4$, $\ell = 16$.

In Figure 6, the relations between fault width and the static offset are shown in more detail. Static offset calculated along the fault centerline, is plotted for the cases $w = 4$ and $w = 1.5$ ($\ell = 8$ in both cases). The horizontal lines show the static solution for an infinitely long strike slip fault (Knopoff, 1958). Except near the end of the fault, the static slip for the finite-length faults is essentially constant along the fault length and is very well predicted from Knopoff's static solution. At the center of the 4 x 8, 1.5 x 8, and 4 x 16 faults, the static slip exceeds the Knopoff solution by less than 5 percent. The "overshoot" phenomenon, observed for the square and circular faults, is not significant over most of the length of the long, narrow faults. This result concurs with the numerical results of Archuleta and Day (1980), which show overshoot confined to within about one half-width of the end of the fault. Elsewhere, the final shear stress is approximately equal to the sliding frictional stress.

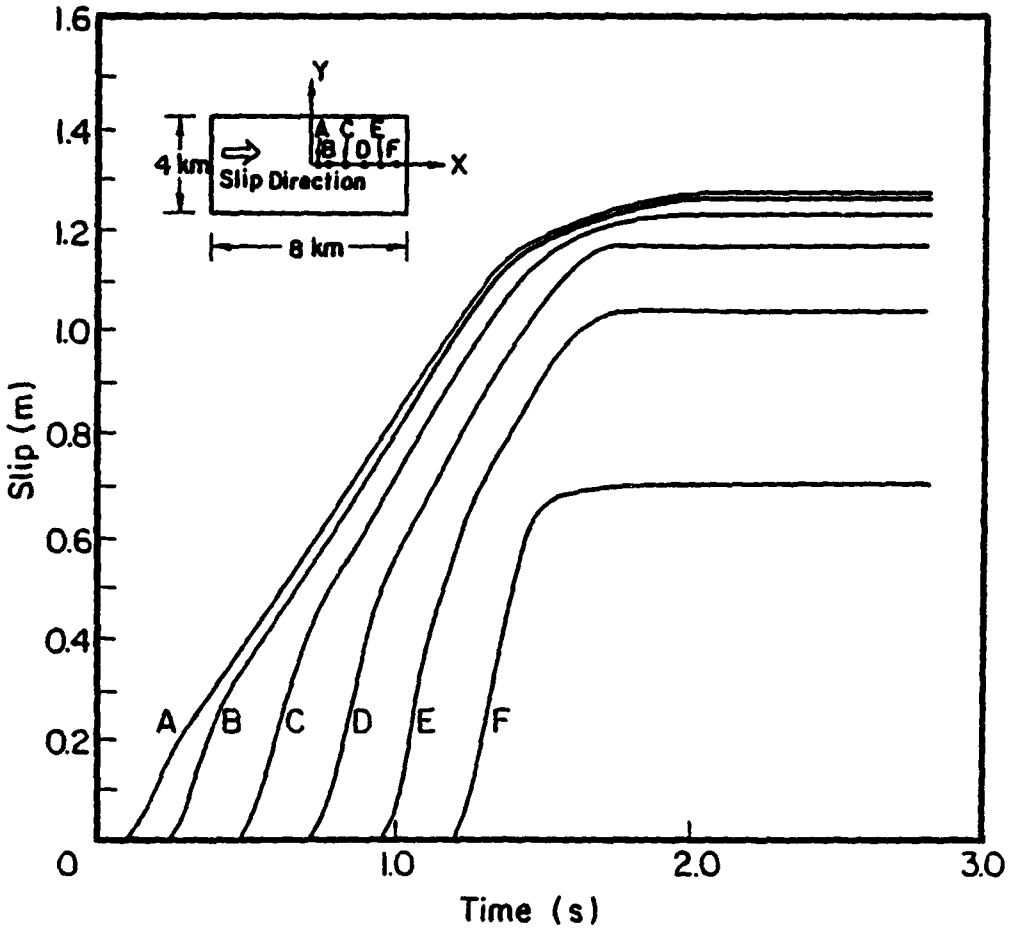


Figure 3. Computed slip time-histories along the center-line of a rectangular fault with aspect ratio 2:1. Scaling is as in Figure 2.

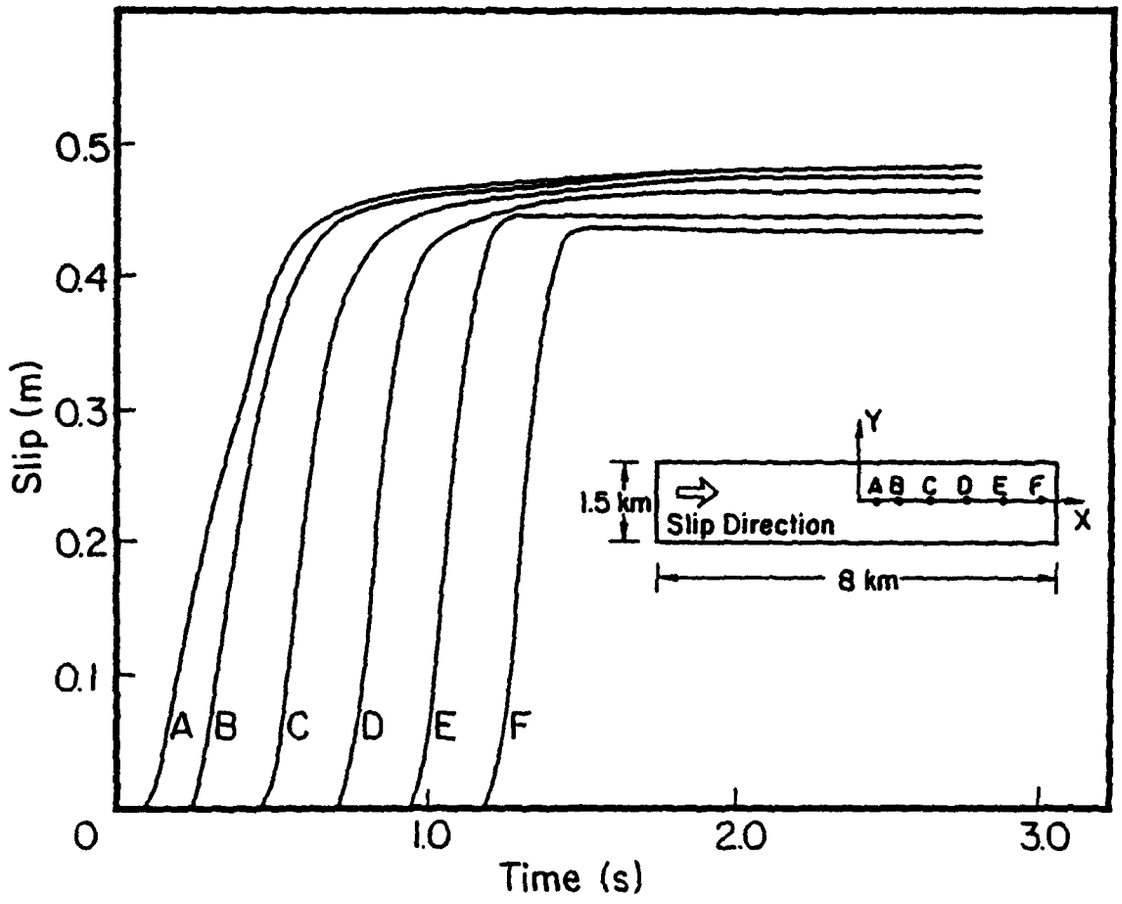


Figure 4. Computed slip time-histories along the center-line of a rectangular fault with aspect ratio 16:3. Scaling is as in Figure 2.

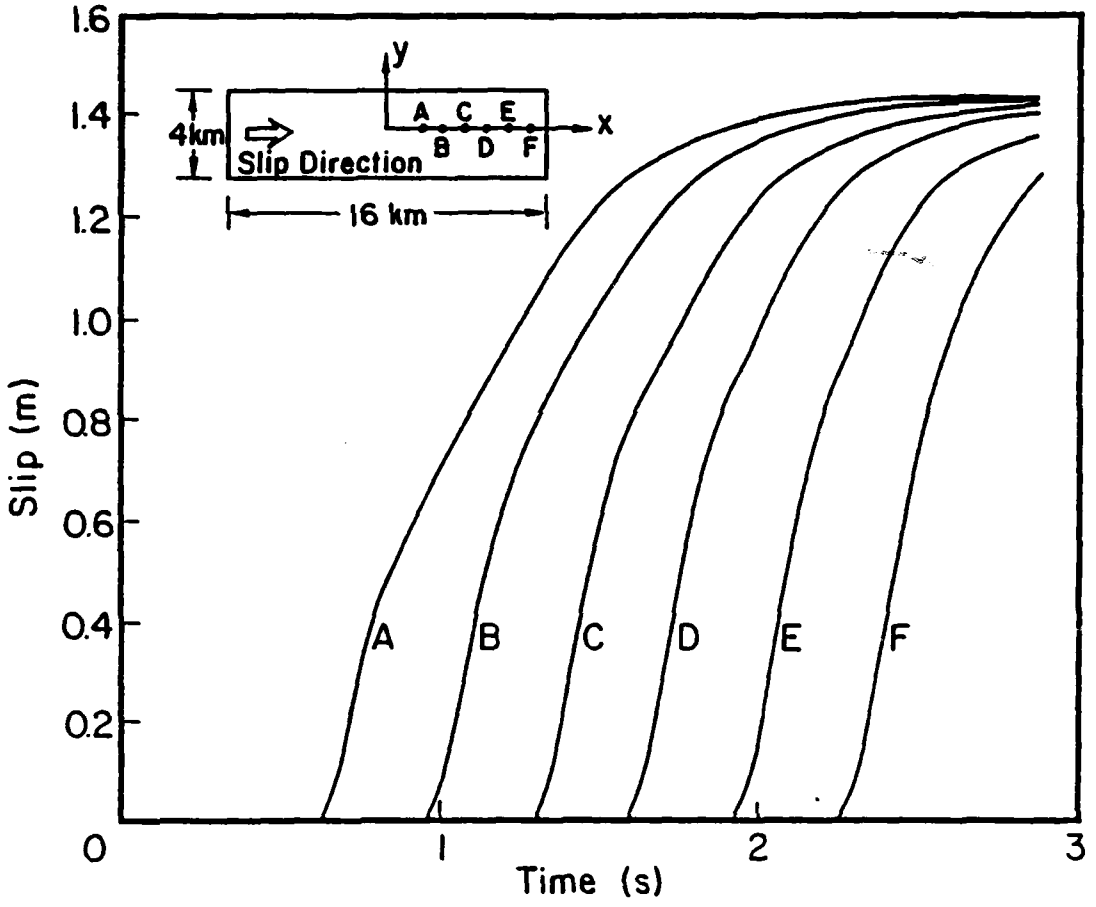


Figure 5. Computed slip time-histories along the center-line of a rectangular fault with aspect ratio 4:1. Slip is scaled to represent a dynamic stress drop of 100 bars and a fault length of 16 km.

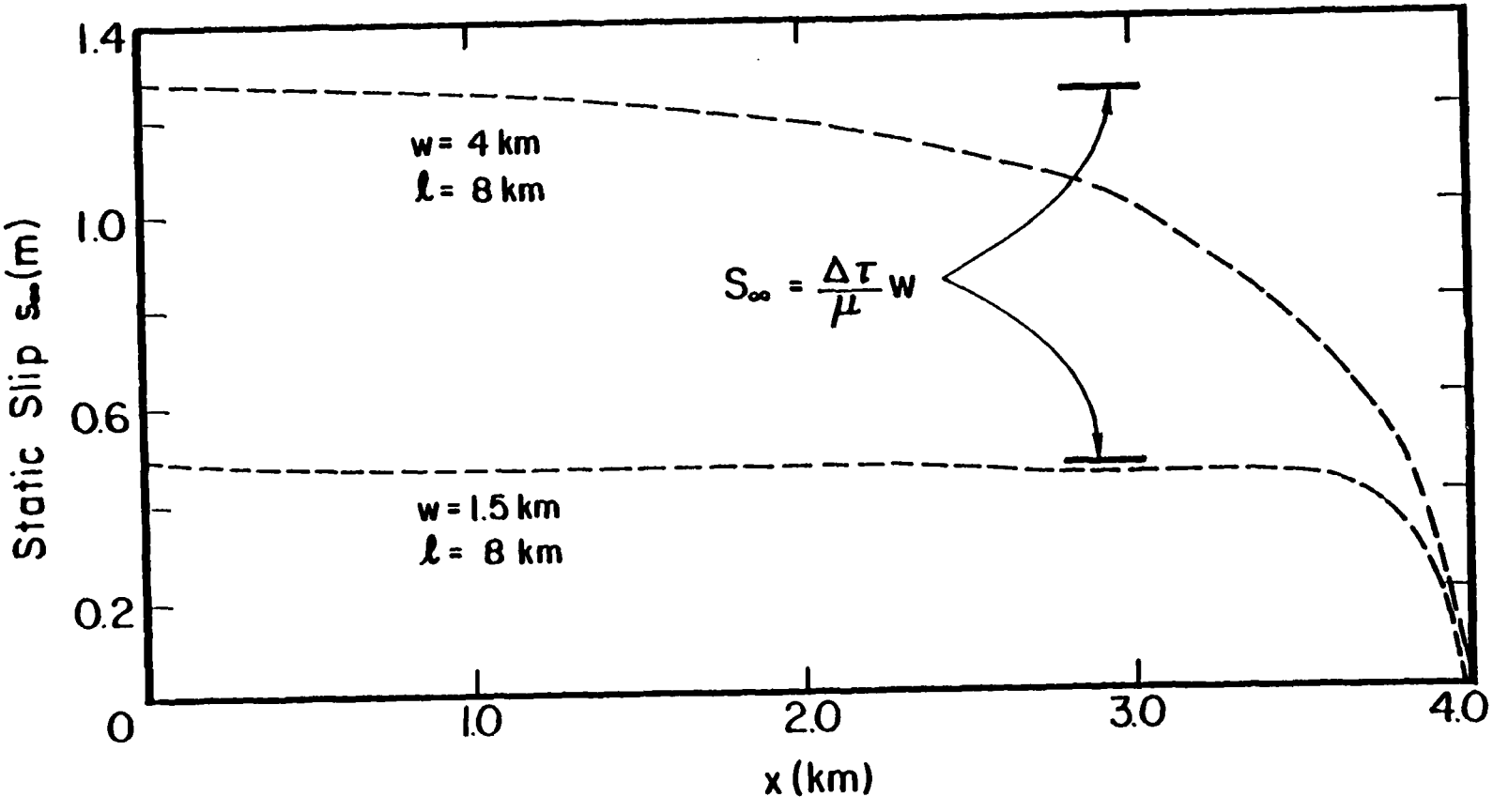


Figure 6. Static slip along the center-line of the fault (x axis), as a function of distance from the hypocenter. Upper curve is for the 4 x 8 km rectangular fault, the lower curve for the 1.5 x 8 km rectangular fault. The horizontal lines are Knopoff's static solution for an infinitely long strike-slip fault.

For a long, narrow fault model, then, the static stress drop will approximately equal the dynamic stress drop $\Delta\tau$, since little or no overshoot occurs, and "undershoot" is not permitted by our model. That is, no physical mechanism has been incorporated into the model (Equation 1) capable of healing the fault at a stress level higher than the prescribed sliding frictional level. In practice, however, we have to be cautious in equating static and dynamic stress drops. Seismic estimates of static stress drop are actually estimates of average static offset divided by gross fault dimension. If an earthquake leaves unbroken patches, or if some regions heal at stress levels above the dynamic friction level, then the seismically inferred static stress drop may be substantially lower than the dynamic stress drop $\Delta\tau$, as demonstrated by Madariaga (1979). Static stress drop estimates may constitute, in general, an approximate lower bound on $\Delta\tau$.

Figure 7 shows the relationship between slip rise time and fault width. Rise time is plotted along the fault centerline for 3 rectangular fault calculations. Rise time in Figure 7 was defined to be the time required for a point on the fault to attain 90 percent of its final value of slip. The horizontal lines represent a rise time equal to the half-width divided by the rupture velocity. For $w = 1.5$, $\ell = 8$, the rise time at first decreases with distance from the hypocenter, then approaches a constant level of about $w/2v_R$. For $w = 4$, $\ell = 16$, a constant level of $w/2v_R$ is again approached as hypocentral distance increases. For $w = 4$, $\ell = 8$, the rise time again decreases with distance from the hypocenter, but the effects of the end of the fault intervene to further reduce the rise time before a constant level can be clearly established. These numerical results predict that a long, narrow fault will have a rise time of roughly $w/2v_R$ over most of its length, with larger values near the hypocenter and lower values near the ends.

Actually, in these simulations the rupture and shear velocities differ only by about 10 percent, so Figure 7 could alternatively be interpreted as showing rise time controlled by $1/\beta$

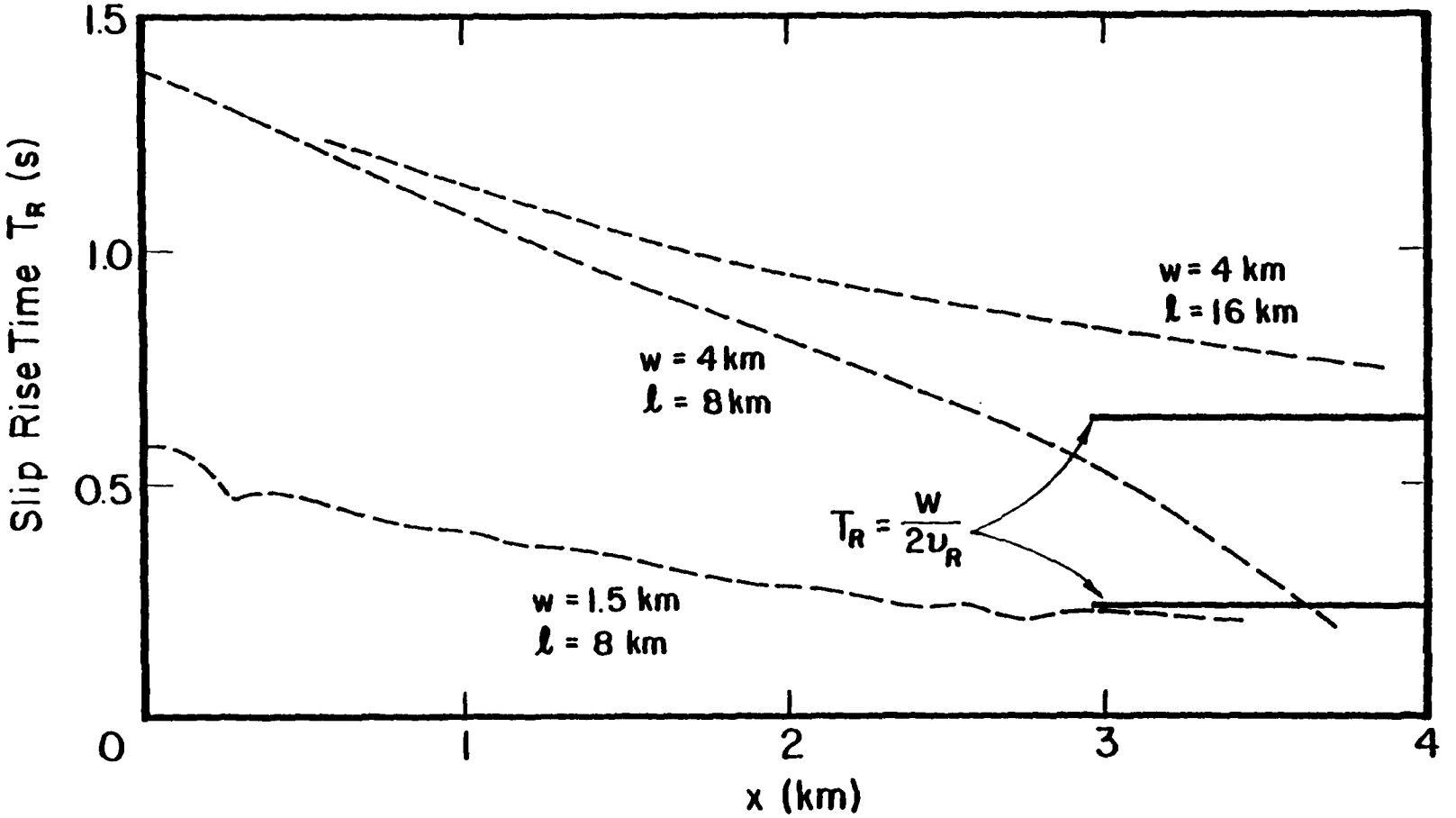


Figure 7. Slip rise time along the center-line (x axis) of rectangular faults. Rise time is defined as the time for slip to reach 90 percent of its final value. Horizontal lines represent rise time equal to the half-width divided by the rupture velocity.

rather than $1/\upsilon_R$. We prefer the latter interpretation, as explained in a later section.

## 3.4 SLIP VELOCITIES

We turn our attention now to the high frequencies. Here it is appropriate to focus on the slip velocity function and, particularly, on the peak slip velocity. Figure 8 shows the slip velocity time histories at selected points along the centerlines of the 4 x 16 km fault model. The slip velocities have been low-pass filtered to remove frequencies in excess of 5 Hz, which is close to the highest frequency that can be reliably computed in the finite difference mesh.

Figure 8 shows that the peak slip velocity initially increases with hypocentral distance. However, the rapid growth in peak slip velocity ceases beyond a hypocentral distance of about one fault width. From then on, the slip velocity function is nearly uniform along the fault centerline. The figure also shows slip velocities observed at points distributed across the fault width, at a fixed distance of 6 km along the length of the 4 x 16 km fault. This figure illustrates the near uniformity of peak slip velocity across the fault width as well as along the fault length, for hypocentral distances greater than about w. The slight decrease in peak slip velocity very near the fault edge, evident in this figure, may be due to the slip function rise time near the edge becoming comparable to the rise time of the 5 Hz low-pass filter.

The uniformity of peak slip velocity is further illustrated in Figure 9. The broken curves represent peak low-passed (5 Hz) slip velocities obtained along the fault centerline for the two cases w = 1.5, $\ell$ = 8 and w = 4, $\ell$ = 16 km, respectively. In both cases, the peak slip velocity first increases rapidly with hypocentral distance, then quickly settles to a uniform level when the hypocentral distance exceeds w. The results in Figure 9 will be further analyzed in the next section.

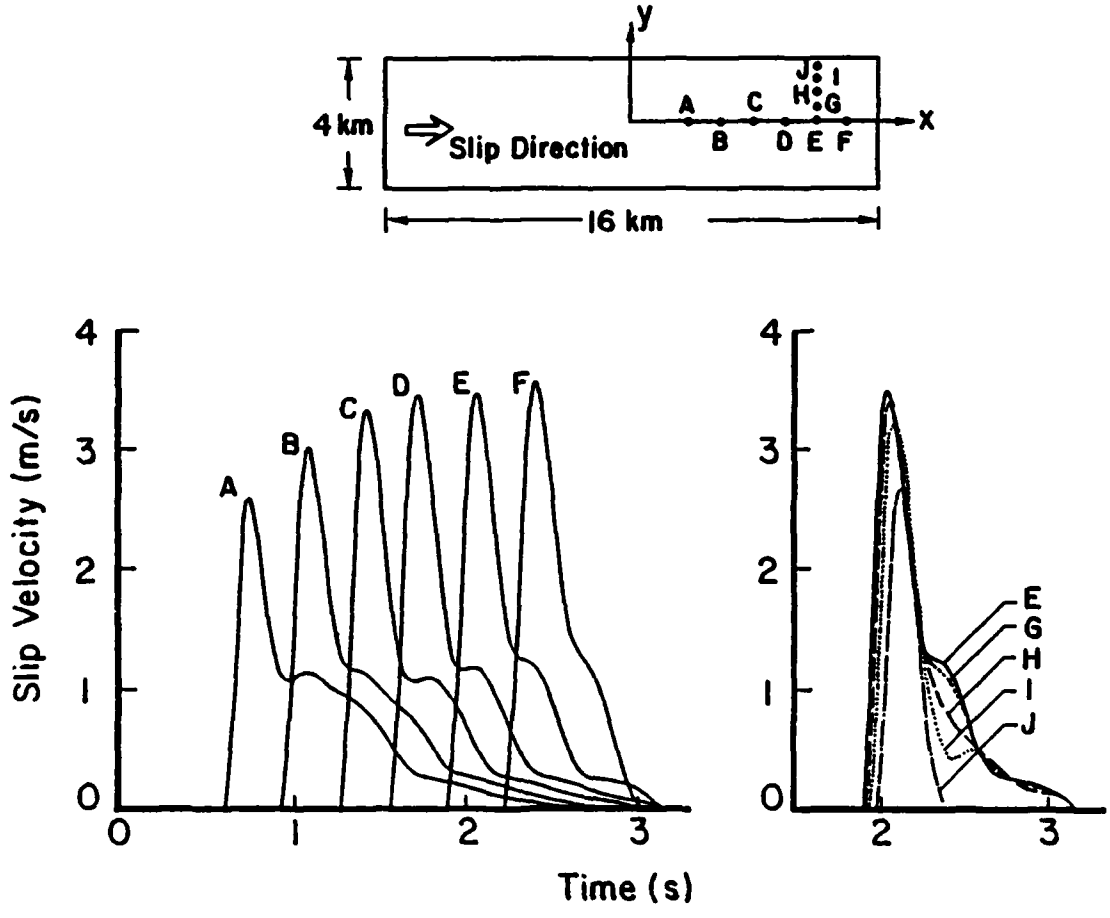


Figure 8. Slip velocity time-histories for the 4 x 16 km fault. The time-histories have been low-pass filtered with a 5 Hz cutoff (corresponding to the limiting frequency for which the numerical method is accurate). Peak slip velocity is nearly invariant with position, for distance x greater than fault width.

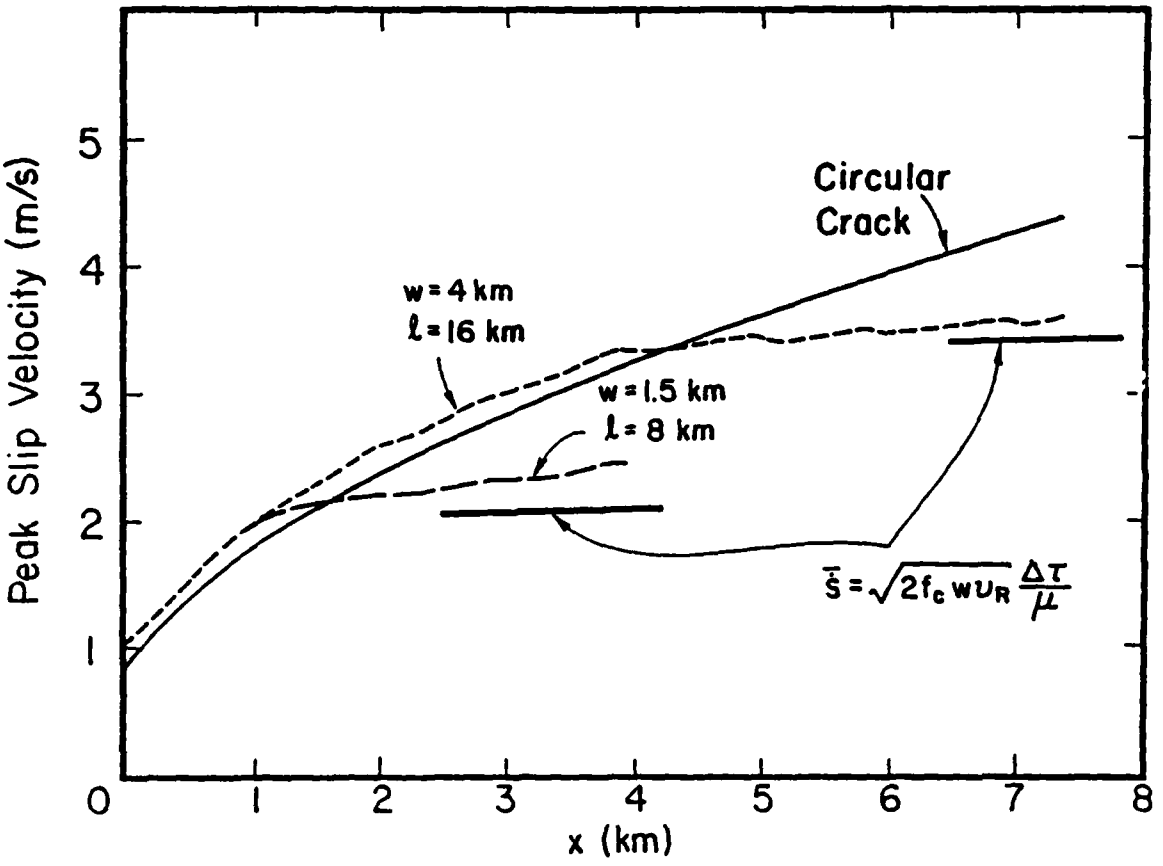


Figure 9. Peak slip velocity as a function of hypocentral distance along the fault center-line (x axis). The dashed curves represent the numerical solutions for 1.5 x 8 km and 4 x 16 km rectangular faults, respectively. The solid curve represents Kostrov's analytical solution for an expanding circular crack. Horizontal lines approximate Kostrov's solution evaluated at radius r = w. Slip velocities for the numerical solutions were digitally low-pass filtered with a 5 Hz cutoff, and the analytical solution was analytically low-passed by convolution with a boxcar function of width $1/f_c$ ($f_c$ = 5 Hz).

# IV. ANALYSIS OF THE SLIP FUNCTION

## 4.1 THE VELOCITY SINGULARITY

We can interpret the numerical results for peak slip velocity by means of the closed-form analytic solution of Kostrov (1964) for an expanding circular crack. The analytic solution for the velocity discontinuity $\dot{s}$ on a circular crack expanding at a uniform rupture velocity is

$$\dot{s} = C \frac{\Delta\tau}{\mu} \beta \frac{T + r/v_R}{\sqrt{T(T+2r/v_R)}} H(T) \qquad (3)$$

where T is the reduced time (time minus rupture arrival time), r is the distance $(x^2 + y^2)^{1/2}$ from the center of the crack to the observation point, H is the unit step function, and C is a constant which equals 0.81 for a Poisson's ratio of 0.25 and rupture velocity of 0.9 $\beta$ (Dahlen, 1974). This solution is singular at the rupture arrival time (except at the hypocenter), and approaches $C\frac{\Delta\tau}{\mu}\beta$ for T large compared to the rupture arrival time. In order to compare this solution to the numerical solutions for finite-width faults, we approximate the effect of a low-pass filter by averaging the analytic solution (Equation 3) over a "cutoff" period $1/f_c$. The resulting expression for peak slip velocity $\bar{\dot{s}}$ on the circular crack is

$$\bar{\dot{s}} = C\frac{\Delta\tau}{\mu} \beta(2rf_c/v_R + 1)^{1/2} \quad , \qquad (4)$$

which, for $f_c >> v_R/r$, is proportional to $r^{1/2}$. That is, in the absence of edge effects (and nonlinearities), peak slip velocity would increase as the square root of distance from the point of rupture.

Equation 4, with $f_c$ equal to 5 Hz, is plotted as a solid curve in Figure 9. Comparing this curve with the peak-velocity curves from the finite-differences fault simulations, we see that

edge effects do not act to modify the peak velocity within a hypocentral distance of approximately one fault width. Up to that distance, the behavior of peak slip velocity closely follows that of Kostrov's expanding circular crack solution, increasing as $r^{1/2}$. The influence of the fault edges is to terminate this growth of peak slip velocity at a hypocentral distance of approximately $r = w$. Thus, the numerical solutions predict that, over most of its length, a long, narrow fault will have a peak slip velocity, after low-pass filtering with cutoff frequency $f_c$, of approximately

$$\dot{\bar{s}} \approx \sqrt{2 f_c w v_R}\ \frac{\Delta\tau}{\mu} \quad . \tag{5}$$

In (5) we have assumed $f_c >> v_R/w$ and have introduced the approximation $C \approx v_R/\beta$, which is accurate within about 10 percent for all sub-shear rupture velocities (Dahlen, 1974). Equation (5) is shown by horizontal lines on Figure 9. For this model of faulting, then, peak (low-passed) slip velocity is proportional to dynamic stress-drop $\Delta\tau$, the square root of rupture velocity, and the square root of fault width.

The above interpretation of the numerical solutions permits us to "undo" the filtering effect of the numerical scheme and characterize the slip velocity singularity at the leading edge of a long, narrow rupture. To simplify the discussion, we take $x>>w$, so that we can ignore the rupture front curvature across the fault width, and so that the rupture front represents Mode II (in-plane shear) crack extension. We expect a singularity of the form

$$\dot{s} \sim V(v_R t - x)^{-1/2}\, H(v_R t - x) \tag{6}$$

This singular form is a universal property of sub-shear-velocity crack propagation (Freund and Clifton, 1974; Freund, 1979). In

Equation (6), V is the velocity intensity, and we can estimate it from Equation (5). Recalling that $\bar{\dot{s}}$ is approximately $\dot{s}$ averaged over time $1/f_c$, and using Equation (6), we obtain the expression

$$V \approx \sqrt{\frac{W}{2}} \frac{\Delta\tau}{\mu} v_R \tag{7}$$

for the velocity intensity. Thus, the model predicts a velocity intensity proportional to the square root of fault width and also proportional to rupture velocity. This result contrasts with two-dimensional crack solutions, in which the velocity intensity is proportional to the square-root of fault length.

In addition, we can use this result to estimate the dynamic stress intensity factor K at the advancing edges of the fault. The shear stress change near the edge, $\tau - \tau_0$, has the asymptotic form (Freund and Clifton, 1974).

$$\tau - \tau_0 \sim K (x - v_R t)^{-1/2} H(x - v_R t). \tag{8}$$

For a Mode II crack, K can be obtained from V (Freund, 1979):

$$K = \frac{2\mu\beta^2}{v_R^3} \frac{R(v_R)}{(1 - v_R^2/\beta^2)^{1/2}} V , \tag{9}$$

where R is the Rayleigh function

$$R(c) = \left[\left(1 - \frac{c^2}{\alpha^2}\right)^{1/2}\left(1 - \frac{c^2}{\beta^2}\right)^{1/2} - \left(1 - \frac{c^2}{2\beta^2}\right)^2\right] .$$

From (7) and (9) we obtain the approximation

$$K \approx \sqrt{2W}\left(\frac{\beta}{v_R}\right)^2 \frac{R(v_R)}{\left(1 - v_R^2/\beta^2\right)^{1/2}} \Delta\tau , \tag{10}$$

so that the dynamic stress intensity factor is proportional to the square root of the fault width and is independent of the length of rupture. This value of K happens to be very close to the dynamic stress intensity factor for a two-dimensional inplane shear crack of length w; in fact, the difference (about 8 percent at $v_R = 0.9\beta$) is not significant in view of the approximate nature of our analysis.

Finally, from Equation (10) we can determine the energy flux into the propagating rupture front, the so-called energy release rate G. G is the energy absorbed per unit area by the advancing crack edge, and is given by (Freund, 1972)

$$G = \frac{\pi}{2v_R} KV ,$$

from which we obtain

$$G \approx \frac{\pi}{2}\left(\frac{\beta}{v_R}\right)^2 \frac{R(v_R)}{\left(1-v_R^2/\beta^2\right)^{1/2}} \frac{\Delta\tau^2}{\mu} w . \qquad (11)$$

That is, for a long, narrow fault, the energy release rate is proportional to the fault width, rather than fault length.

## 4.2 THE STATIC SLIP

From Figure 6, it was observed that the final slip for the rectangular fault model is very close to Knopoff's two-dimensional (antiplane) static solution, except near the ends of the fault. Comparing the two cases shown in that figure, it is evident that the length of the end region is proportional to fault width, rather than fault length. The greatest deviation from the two-dimensional solution occurs within a distance w/2 of the ends. We use these observations to construct an approximate expression which summarizes the numerical results.

Figure 10 shows in more detail the numerical results for static slip on the fault with aspect ratio 2. Four profiles across the narrow dimension of the fault are shown as dashed curves. The

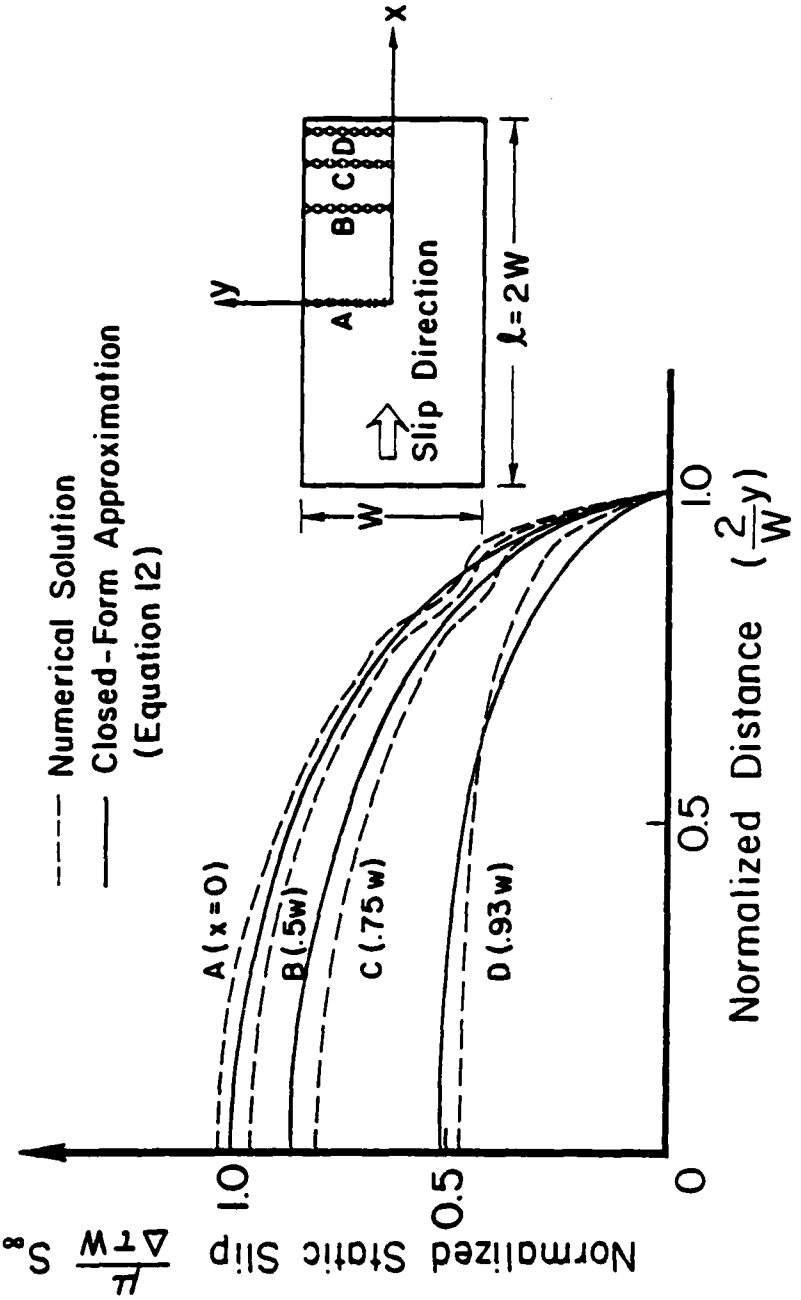


Figure 10. Comparison of numerical solution and closed-form approximation (Equation 12) for the static slip on a fault with aspect ratio 2:1.

uppermost solid curve is Knopoff's static solution for the infinitely long (in the x direction) fault of width w:

$$s(y) = \frac{\Delta\tau}{\mu} w \left[ 1 - \left(\frac{2y}{w}\right)^2 \right]^{1/2}$$

For points more than half a fault width away from the end of the fault, this expression is a reasonable approximation to the numerical solution; for x = 0 and x = 0.5w, the agreement is within about 10 percent over most of the fault width. To modify this expression to account for end effects, we are motivated by the fact that, very near the fault ends, plane-strain conditions should be approximated. Therefore, guided by the two-dimensional static solution of Starr (1928) for a finite, in-plane shear crack, and the observation that the end region is of length approximately w/2, we try the approximation

$$s_\infty = \frac{\Delta\tau}{\mu} w \left[ 1 - \left(\frac{2y}{w}\right)^2 \right]^{1/2} \quad (2-\xi)^{1/2} \; \xi^{1/2} , \qquad (12)$$

where $\xi(x)$ is 1 for points farther than w/2 from the ends, and otherwise is the normalized distance to the end of the fault:

$$\xi(x) = \begin{cases} \frac{2}{w} |\ell - x| & \text{if } |\ell - x| < \frac{w}{2} \\ 1 & \text{if } |\ell - x| \geq \frac{w}{2} \end{cases} .$$

The approximation (12) is simply that the static slip has the value $\frac{\Delta\tau}{\mu} w$ along the centerline, with an elliptical cross-section across the width, multiplied by a quarter-ellipse taper near each end. As Figure 10 indicates, Equation 12 represents the numerical solutions fairly well over the whole length and width of the fault, though somewhat less well near the end.

To summarize, we find that final slip for a long, narrow fault is proportional to fault length rather than fault width. The final slip is well approximated by Knopoff's solution, except near the

ends. The extent of this end region is also proportional to fault width, not length. Equation 12 represents reasonably well the overall behavior of the static offset.

### 4.3 THE SLIP RISE TIME

The approximate expressions deduced above for the slip velocity singularity and static slip can be used to derive an approximate expression for the rise time $T_R$. Integrating the slip velocity singularity (Equations 6 and 7) and equating the resulting slip to the static slip (Equation 12) gives the following prediction for the rise time:

$$T_R = \frac{w}{2v_R}\left[1 - \left(\frac{2y}{w}\right)^2\right](2 - \xi)\ \xi, \qquad (13)$$

assuming $x>>w$. This derivation of Equation (13) assumes that the slip velocity at a point follows Equation 6 until the static slip value is reached, then slip terminates abruptly. This is an oversimplification of the actual slip function, as Figure 8 shows. However, the resulting expression for $T_R$ is in very good agreement with the numerical result, shown in Figure 7, that the rise time along the fault centerline ($y=0$) approaches $w/2v_R$ for points more than one fault width away from the hypocenter. Furthermore, the numerical result that $T_R$ increases with decreasing hypocentral distance for $x<w$, which is evident in Figure 7, can be interpreted in the same manner. For $x<w$, however, Equation (6) should be replaced by Equation (3) to estimate the rise time.

It is perhaps surprising that Equation 13 involves the rupture velocity, rather than the shear-wave velocity, since the arrival of shear waves diffracted from the long edges of the fault might be expected to control the rise time at a point on the fault. In fact, both Day (1979) and Das (1981) have adequately explained rise times for numerical models of rectangular faults on the basis of diffracted shear-wave arrivals, predicting rise time proportional to $1/\beta$. Since the shear and rupture velocities differ by only 10 percent or so in our simulations, we could not distinguish between a

$1/\beta$ and $1/v_R$ dependence for $T_R$ on the basis of these numerical results alone. Instead, the proportionality of rise time to the reciprocal of rupture velocity in Equation 13 follows directly from the property that the velocity intensity at the leading edge of the fault is proportional to $v_R$. This proportionality to $v_R$ is a general property of dynamic cracks running at sub-Rayleigh velocity (see, for example, Freund, 1976). Therefore, it will take longer for a slow-running crack to reach static equilibrium than for a fast-running crack to do so (recall that negligible static overshoot was found for the long, narrow faults and that static shear stress is required by the model to be less than or equal to $\tau_f$). The shear-wave diffraction effect may act to retard the slip velocity below that given by (6) and (7), but not to increase it. For our earthquake model, then, an expression such as Equation (13) is a more appropriate approximation to the rise time than would be obtained with $\beta$ in place of $v_R$. The conclusion might be different if some mechanism, such as velocity-dependent friction (Dieterich, 1978) were incorporated into the fault model to permit healing to occur at a stress level substantially higher than $\tau_f$.

## V. SUMMARY AND DISCUSSION

The approximate behavior of the slip function for a long, narrow fault, as deduced from the foregoing analysis of the numerical solutions, is summarized schematically in Figure 11. Near the hypocenter, the slip function initially resembles Kostrov's solution, Equation (3), in which the velocity singularity grows as the square root of hypocentral distance. For x (distance along the fault length) greater than the fault width w, this growth of the velocity singularity ceases, and the slip function is then nearly invariant with distance in the x direction, except near the ends.

In this "steady-state" regime, $x > w$, both rise time and static slip are proportional to w, and the advancing crack edges have velocity singularities proportional to $\sqrt{w}$. Slip nearly ceases at a given point after the crack edge has advanced a distance of roughly one half-width past the point. The slip-velocity time function can be approximated by

$$\dot{s} = \sqrt{\frac{w}{2} \upsilon_R} \quad \frac{\Delta\tau}{\mu} \quad T^{-1/2} \left[ H(T) - H(T-T_R) \right]. \tag{14}$$

In Equation 14, T is reduced time $t-\upsilon_R/r$, and $T_R$ is the slip rise time as given by Equation 13. This approximation is sketched (for the case $y = 0$) in Figure 12 along with the corresponding shear-stress singularity. Also shown for comparison in Figure 12 is a numerical solution for slip velocity (point E of Figure 8).

The low-frequency characteristics obtained here for the slip function, that is, rise time and static slip, are similar to those inferred from similar calculations by Archuleta and Day (1980) and from a spontaneous-rupture numerical model by Das (1981). The mesh refinement used to obtain the numerical solutions in this study, however, has permitted observation of some previously unresolved high-frequency characteristics of the solution, as well. These high-frequency slip characteristics, specifically the strength of

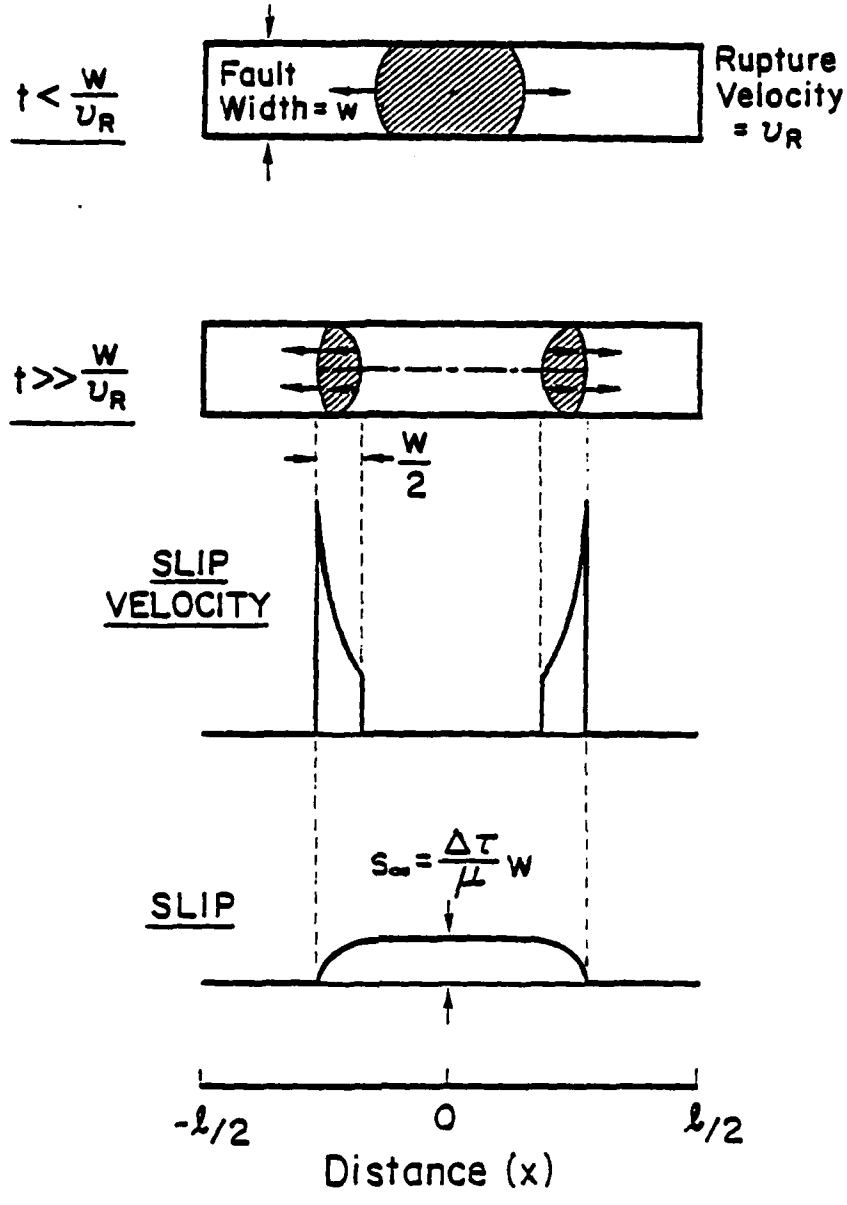


Figure 11. Sketch summarizing the approximate behavior of the slip function for long, narrow faults. At a time greater than that required for the rupture to cross the fault width ($\frac{W}{v_R}$), slip is concentrated on two patches, each approximately one half-width long, moving away from the hypocenter in opposite directions. The shape of slip function then remains nearly invariant as these patches propagate along the fault length. In this steady-state regime, the static slip and rise time are proportional to w, and the slip velocity has a square root singularity with intensity proportional to $\sqrt{w}$.

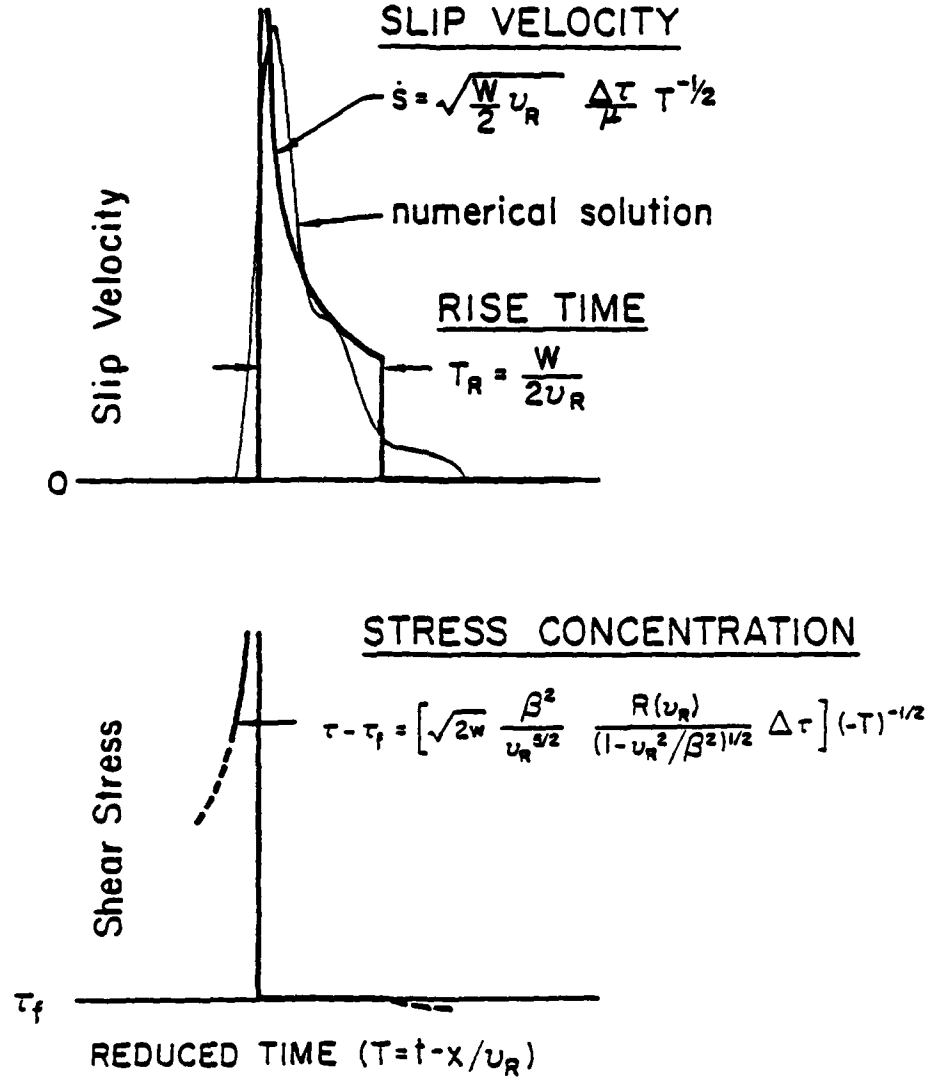


Figure 12. Sketch of a closed-form approximation for the slip velocity time-history (Equation 14) at y = 0, x >> w, compared to a corresponding numerical solution (point E of Figure 8). Also sketched is the corresponding approximation derived for the shear-stress singularity (Equations 8 and 9).

the velocity and stress singularities at the leading edge of the fault, are of particular importance for understanding the radiation of high-frequency seismic energy. For example, Madariaga (1977a) has shown that "the high frequencies originate from the stress and slip velocity concentrations in the vicinity of the fault's edges". Frequencies in excess of 1 Hz are an important component of the strong ground motion recorded in the immediate vicinity of earthquakes, and are also of importance for understanding earthquake ground motion at regional distances, where substantial seismic energy is observed in the 1-5 Hz range.

We first consider some implications of the dynamic solutions for kinematic modeling procedures used to predict ground motion time histories. An assumption commonly made in kinematic modeling of earthquake ground motion is that the source can be represented by a uniform dislocation, that is, a slip function which is uniform in its amplitude and its time dependence over the entire fault plane (apart from a time delay associated with the rupture arrival time). Usually the slip function is assumed to have a simple ramp time-history, i.e., constant slip velocity over some specified rise time. We focus for now on the high-frequencies radiated from the leading edge of the fault after it has propagated more than a fault width from the hypocenter. In this case, Equation (14) is an appropriate representation of the slip function for our dynamic solutions. The spectral amplitude of a ramp function behaves asymptotically at high frequency as $f^{-1}$, whereas Equation 14 implies an $f^{-1/2}$ slip-function spectrum (Lighthill, 1958, p. 52). Since the predicted radiation depends linearly on the assumed slip function, we would expect the ramp-function source representation to be relatively deficient in its prediction of high-frequency ground motion. For example, one might attempt to approximate the slip function using a ramp function in which the ratio of static slip to rise time is the same as for the dynamic solution (Equation 14).

Then, at a period of $T_R/10$, the ramp slip function would be deficient in spectral content by about a factor of 7 relative to Equation 14.

This spectral comparison between the ramp-function representation and the dynamic solution may provide a physical basis for a result obtained by Del Mar Technical Associates (1979). They modeled the 1966 Parkfield earthquake using a uniform-dislocation earthquake model with a ramp slip function, attempting to fit spectral characteristics of the ground motion recorded at the 5 accelerograph stations of the Chalome-Shandon array. They reported difficulty in matching observed response spectra over a broad period range with this slip function; in order to fit recorded short-period spectral levels of ground motion, it was necessary to tolerate a large overestimate at long periods. This result is in accord with our prediction that the ramp function earthquake representation is relatively deficient in high frequencies.

Of course, a ramp function suitably scaled, might be adequate for modeling ground motion over a narrow frequency band. As an example, Bouchon (1979) successfully synthesized the velocity and displacement pulses recorded for the Parkfield event at Station 2, using a uniform slip function with a ramp time history. In this case, however, the predominant period of the waveforms being modeled was several times greater than the assumed rise time of the ramp.

The dynamic solutions reveal a second difficulty with uniform-dislocation kinematic models, this one involving the starting phase radiated from the hypocenter when rupture initiates. We have seen that the ramp function is a poor representation of the slip function for the dynamic solution at points well removed from the hypocenter. It is tempting to try to retain the uniform dislocation approximation, but alter the time-function to resemble the singular behavior of the dynamic solution in the "steady-state" regime, $x>>w$. Unfortunately, if the time-function of a uniform dislocation model is chosen to match the the dynamic solution at points far from

the hypocenter (i.e., replace the ramp function by an expression such as (14)), then the starting phase predicted for the uniform dislocation will be much larger than that for the dynamic model. To see this, we use the expression derived by Richards (1973) for the first-motion approximation to the shear-wave acceleration $\underline{\ddot{u}}_s$ due to an expanding circular crack:

$$\underline{\ddot{u}}_s = \underline{R} \frac{C\upsilon_R^2}{R\left(1-\upsilon_R^2/\beta^2 \sin^2\theta\right)^2} \frac{\Delta\tau}{\mu} H(t-R/\beta) \qquad (15)$$

where $\underline{R}$ contains the double couple radiation pattern, $\theta$ is the angle formed at the hypocenter by the fault normal and the receiver direction, and R is the hypocentral distance to the receiver. We will also use the corresponding expression for an expanding, uniform, circular dislocation:

$$\underline{\ddot{u}}_s = \underline{R} \frac{\upsilon_R^2}{2\beta R\left(1-\upsilon_R^2/\beta^2 \sin^2\theta\right)^{3/2}} \dot{s}(t-R/\beta) , \qquad (16)$$

where $\dot{s}(t)$ is the assumed slip-velocity time function for the uniform dislocation. Equation (16) can be deduced from Savage (1966). If, in a uniform-dislocation model, we choose $\dot{s}$ in accordance with Equation 14, Equation 16 implies that the acceleration first-motion will have a $T^{-1/2}$ singularity, whereas the dynamic solution for the initiation phase, Equation 15, gives only a step discontinuity for $\underline{\ddot{u}}_s$. To quantify further the effect of the uniform-dislocation approximation in this case, assuming a band-limited observation with cutoff frequency $f_c$, we substitute Equation 14 into Equation 16, average over a period $1/f_c$, and take the ratio of (16) to (15). The result is that the uniform dislocation yields a starting acceleration phase which exceeds the dynamic solution by a factor of $\sqrt{(1-\frac{\upsilon_R^2}{\beta^2}\sin^2\theta)T_R f_c}$ (we have introduced the approximation $T_R \approx w/2\upsilon_R$ and $\upsilon_R/\beta \approx C$). Thus, for periods much less than the rise

time, the uniform dislocation model substantially over-predicts the starting phase amplitudes, relative to the dynamic solution (except near $\theta = 90°$).

In summary, the uniform dislocation kinematic models, since they do not incorporate the spatial variation of slip present in the dynamic solution for $x<w$, will either over-predict the starting phase or under-predict the dominant high-frequencies associated with the velocity singularity. At least for the simple dynamic model studied here, we can't construct a uniform dislocation approximation which will replicate both the starting phase radiation and the high-frequency behavior of slip at the leading edge of the fault.

The numerical solutions obtained here also have tectonophysical implications. Husseini, et al (1975), Das and Aki (1977b), and Aki (1979) have analyzed the role of fault-plane "barriers", or high-strength segments, in resisting or arresting rupture growth. Whether fault growth stops at a barrier or rupture continues through the barrier depends upon the barrier strength, as well as upon the stress intensity factor developed at the leading edge of the fault. In two-dimensional fracture mechanics, the stress intensity increases with rupture growth as the square root of fault length, for a given dynamic stress drop. Therefore, one would predict that as fault length increased, the likelihood of rupturing barriers would increase as well. In contrast, the three-dimensional solutions demonstrate that the stress intensity ceases to grow with fault length beyond a distance of about one fault width. Equation (10), derived on the basis of the three-dimensional numerical solutions, gives a stress intensity factor proportional to the square-root of fault width. The capability of a long narrow fault to rupture barriers should be proportional to dynamic stress drop, and the square-root of fault width, but independent of rupture length.

Similarly, two-dimensional analytical and numerical solutions imply that the energy release rate at the fault edge increases with fault length. As Andrews (1976) points out, those results would

require that longer ruptures be accompanied by thicker zones of microcracking or other inelastic response. Our three-dimensional results, however, imply an energy release rate proportional to width, rather than length (Equation 11). So we conclude that the level of inelastic response associated with long, narrow ruptures will depend on fault width, not length.

The numerical results also have important potential applications to the problem of seismic monitoring of nuclear test-limitation treaties. For example, some of the methods proposed for discriminating earthquakes from underground explosions make use of characteristic spectral differences in the radiation from the two types of events (e.g., Bache, et al., 1979). Results such as these can help provide a theoretical basis for such discriminants.

A second example relates to the seismic estimation of explosion yield. This problem requires a good understanding of propagation effects on the seismic signal, particularly the average path attenuation (i.e., t*). Anelastic attenuation is difficult to separate observationally from source effects, however. In order to make use of earthquake signals to infer propagation-path attenuation, it is therefore important to have a good earthquake source model, a point also underscored by Hanks (1981). To address these questions using the numerical simulations, it will be necessary to compute the radiated seismic signal from the earthquake models. The slip histories obtained here are sufficient for synthesizing the radiated waveforms, and this will be undertaken in a subsequent report.

## VI. REFERENCES


Aki, K. (1979). Characterization of barriers on an earthquake fault, J. Geophys. Res., 84, 6140-6148.

Andrews, D. J. (1976). Rupture propagation with finite stress in antiplane strain, J. Geophys. Res., 81, 3575-3582.

Apsel, R. J. (1979). Dynamic Green's functions for layered media and applications to boundary-value problems, Ph.D. dissertation, University of California, San Diego,

Archuleta, R. J. (1976). Experimental and numerical three-dimensional simulations of strike-slip earthquakes, Ph.D Dissertation, University of California, San Diego.

Archuleta, R. J. and J. N. Brune (1975). Surface strong motion associated with a stick-slip event in a foam rubber model of earthquakes, Bull. Seism. Soc. Am., 65, 1059-1071.

Archuleta, R. J. and G. A. Frazier (1978). Three-dimensional numerical simulations of dynamic faulting in a half-space, Bull. Seis. Soc. Am., 68, 573-598.

Archuleta, R. J. and S. M. Day (1980). Dynamic rupture in a layered medium: The 1966 Parkfield earthquake, Bull. Seis. Soc. Am., 70, 671-689.

Bache, T. C., S. M. Day and J. M. Savino (1979), "Automated Magnitude Measures, Earthquake Source Modeling, VFM Discrimination Testing and Summary of Current Research," Systems, Science and Software Quarterly Technical Report SSS-R-79-3933, Submitted to the Advanced Research Projects Agency, February.

Bouchon, M. (1979). Predictability of ground displacement and velocity near an earthquake fault: An example: The Parkfield earthquake of 1966, J. Geophys. Res., 84, 6149-6156.

Brune, J. N. (1970). Tectonic stress and the spectra of seismic shear waves from earthquakes, J. Geophys. Res., 75, 4997-5009.

Burridge, R., and J. R. Willis (1969). The self-similar problem of the expanding elliptical crack in an anisotropic solid, Proc. Camb. Phil. Soc., 66, 443-468.

Byerlee, J. D. (1967). Frictional characteristics of granite under high confining pressures, JGR, 72, 3639-3648.

Cherry, J. T. (1977). Users' manual for the TRES code, Systems, Science and Software Report SSS-R-77-3128.

Cherry, J. T., E. J. Halda, and K. G. Hamilton (1976). A deterministic approach to the prediction of free field ground motion and response spectra from stick-slip earthquakes, Earthquake Eng. Struct. Dyn., 4, 315-332.

Dahlen, F. A. (1974). On the ratio of P-wave to S-wave corner frequencies for shallow earthquake sources, Bull. Seism. Soc. Am., 64, 1159-1180.

Das, S. (1980). A numerical method for determination of source time functions for general three-dimensional rupture propagation, Geophys. J., 62, 591-604.

Das, S. (1981). Three-dimensional spontaneous rupture propagation and implications for the earthquake source mechanism, Geophys. J., in press.

Das, S. and K. Aki (1977a). A numerical study of two-dimensional spontaneous rupture propagation, Geophys. J. R., 50, 643-668.

Das, S. and K. Aki (1977b). Fault plane with barriers: a versatile earthquake model, J. Geophys. Res., 82, 5658-5670.

Day, S. M. (1977). Finite element analysis of seismic scattering problems, Ph.D. dissertation, University of California, San Diego.

Day, S. M. (1979). Three-dimensional finite difference simulation of fault dynamics, Final Report SSS-R-80-4295, Systems, Science and Software, La Jolla, CA.

Del Mar Technical Associates (1979). Simulation of earthquake ground motions for San Onofre Nuclear Generating Station, Unit 1: Supplement I, Rept. for Southern California Edison Company, submitted for review to the Nuclear Regulatory Commission.

Dieterich, J. H. (1972). Time-dependent friction in rocks, J. Geophys. Res., 77, 3690-3697.

Dieterich, J. H. (1978). Time-dependent friction and the mechanics of stick-slip, Pure and Appl. Geophys., 116, 790-806.

Dieterich, J. H., D. W. Barber, G. Conrad and Q. A Gordon (1978). Preseismic slip in a large scale friction experiment, Proceedings of the 19th U. S. Rock Mechanics Symposium, Mackay School of Mines, University of Nevada, Reno.

Eshelby, J. D. (1969). The elastic field of a crack extending non-uniformly under general anti-plane loading, J. Mech. Phys. Solids, 17, 177-199.

Fossum, A. F., and L. B. Freund (1975). Non-uniformily moving shear crack model of a shallow focus earthquake mechanism, J. Geophys. Res., 80, 3343-3347.

Freund, L. B. (1972). Energy flux into the tip of an extending crack in an elastic solid, J. Elasticity, 2, 341-348.

Freund, L. B. (1976). The analysis of elastodynamic crack tip stress fields, in Mechanics Today, 3, 55-91, ed. Nemat-Nasser, S., Pergamon Press, New York.

Freund, L. B. (1979). The mechanics of dynamic shear crack propagation, J. Geophys. Res., 84, 2199-2209.

Freund, L. B. and R. J. Clifton (1974). On the uniqueness of plane elastodynamic solutions for running cracks, J. Elasticity, 4, 293-299.

Hanks, T. C. (1981), "The Corner Frequency Shift, Earthquake Source Models, and Q," BSSA, 71, pp. 597-612.

Haskell, N. A. (1964). Total energy and energy spectral density of elastic wave radiation from propagating faults, Bull. Seism. Soc. Am., 54, 1811-1841.

Haskell, N. A. (1969). Elastic displacements in the near-field of a propagating fault, Bull. Seism. Soc. Am., 59, 865-908.

Husseini, M. I., D.B. Jovanovich, M. J. Randall, and L. B. Freund (1975). The fracture energy of earthquakes, Geophys. J., 45, 367-385.

Keller, J. B. (1962). Geometrical theory of diffraction, J. Opt. Soc. Am., 52, 116-130.

Knopoff, L. (1958). Energy release in earthquakes, Geophys. J., 1, 44-52.

Kostrov, B. V. (1964). Self-similar problems of propagation of shear cracks, J. Appl. Math. Mech., 28, 1077-1087.

Kostrov, B. V. (1966). Unsteady propagation of longitudinal shear cracks, J. Appl. Math. Mech., 30, 1241-1248.

Kostrov, B. V. (1970). The theory for the focus for tectonic earthquakes, Izv., Earth Phys., 4, 258-267.

Kostrov, B. V. (1975). On the crack propagation with variable velocity, Int. J. of Fracture, 11, 47-56.

Lighthill, M. J. (1958). Fourier Analysis and Generalised Functions, Cambridge University Press, Cambridge, England.

Madariaga, R. (1976). Dynamics of an expanding circular fault, Bull. Seism. Soc. Am., 66, 639-666.

Madariaga, R, (1977a). High-frequency radiation from crack (stress-drop) models of earthquake faulting, Geophys. J., 51, 625-651.

Madariaga, R. (1977b). Modelling of three-dimensional earthquake faults by finite differences (abstract), EOS Trans. AGU, 58, 1191.

Madariaga, R. (1978). The dynamic field of Haskell's rectangular dislocation fault model, Bull. Seis. Soc. Am., 68, 869-887.

Madariaga, R (1979). On the relation between seismic moment and stress drop in the presence of stress and strength heterogeneity, J. Geophys. Res., 84, 2243-2250.

Neuber, H., (1937). Kerbspannungslehre, Springer-Verlag, Berlin; Theory of notch stresses: Principles for exact calculation of strength with reference to structural form and material, the Office of Tech. Info., AEC-tr-4547, 1958 (English translation).

Richards, P. G. (1973). The dynamic field of a growing plane elliptical shear crack, Intern. J. Solids Struct., 9, 843-861.

Savage, J. C. (1966). Radiation from a realistic model of faulting, Bull. Seism. Soc. Am., 56, 577-592.

Scholz, C. H., P. Molnar, and T. Johnson (1972). Detailed studies of frictional sliding of granite and implications for the earthquake mechanism, JGR, 77, 6392-6406.

Starr, A. T. (1928). Slip in a crystal and rupture in a solid due to shear, Proc. Camb. Phil. Soc., 24, 489-500.

Wiggins, R. A., G. A. Frazier, J. Sweet and R. Apsel (1978). Modeling strong motions from major earthquakes, Proceedings of the Second International Conference on Microzonation for Safer Construction - Research and Application, San Francisco, California, November 26 - December 1, 1978, 693-700.

Wu, F. T., K. C. Thomson, and H. Kuenzler (1972). Stick-slip propagation velocity and seismic source mechanism, Bull. Seism. Soc. Am., 62, 1621-1628.